Supplementary Material

Advanced Bifunctional bionic neural network-like architecture constructed by multi-scale carbon nanotubes nanocomposites

Shuaizhen Li [1, 2], Tianwen Xie [1, 2], Lin Ma [1, 2], Daheng Liu [1, 2], Nan Huang [1], Wei Liu [1], Bing Li[1], Zhigang Gai[4], Xin Jiang[3], Song Ma [1, *] and Zhidong Zhang [1]

[1] *Shenyang National Laboratory for Materials Science, Institute of Metal Research, Chinese Academy of Sciences 72 Wenhua Road, Shenyang 110016, China*

[2] *School of Materials Science and Engineering, University of Science and Technology of China, 72 Wenhua Road, Shenyang 110016, China*

[3] *Institute of Materials Engineering, University of Siegen, No.9-11 Paul-Bonatz-Str., Siegen, 57076 Germany*

[4] *Institute of Oceanographic Instrumentation, Qilu University of Technology (Shandong Academy of Sciences), Qingdao, 266100, China*

**Song Ma. E-mail: songma@imr.ac.cn*

Preparation of Ni_3Fe@NCNT@CF architecture

Ni_3Fe@NCNT@CF architecture were prepared via a facile vacuum dip-coating and a subsequent carbonization process. MF (2×2×2 cm^3) was cleaned ultrasonically with anhydrous ethanol and deionized water and dried. Subsequently, MF was transferred to NaOH solution (5 mol·L^{-1}) a t 65 °C for 30 min for roughening its surface. Then the pretreated MF was immersed into 1 wt% chloride salt ($FeCl_3·6H_2O$ and $NiCl_2·6H_2O$) mixed solution for 24 h to chelate with Fe^{3+} and Ni^{2+} and was washed with deionized water for several times. Subsequently, the foams were vacuum-dried at 90°C for 24h. Finally, the foams were pyrolyzed under Ar atmosphere at different temperatures (700 °C, 800 °C and 900 °C) for 2 h to obtain the Ni_3Fe@NCNT@CF architecture (labeled as NNCF-1, NNCF-2, NNCF-3, respectively).

Anti-corrosion Performance Measurements

The working electrode was obtained by dropping the mix solution, including NNCF-2, Nafion solution and ethanol, on a glassy carbon electrode with 4 mm diameter. The potentiodynamic polarization curve was recorded in a potential window from −0.4 to 0.6 V at a scan rate of 10 mV s^{-1}. EIS was performed in a frequency range from 100 kHz to 0.01 Hz.

Radar Cross Section (RCS) Simulation

The far-field response RCS values were simulated using CST Studio Suite 2019. The simulation model used a 180 mm square composed of an upper absorbing layer

(Ni_3Fe@NCNT@CF, 2 mm) and a bottom perfect electric conductor layer (PEC, 1 mm). The model plate was placed on the XOY plane, and the selected field monitor frequency was 17 GHz. For a certain scattering source, it is generally accepted that the scattering directions of RCS value (σ) can be determined by θ and φ, which can be described as:

$$\sigma(dBm^2) = 10\log\left[\frac{4\pi S}{\lambda^2}\left|\frac{E_s}{E_i}\right|^2\right] \quad (1)$$

where, S, λ, E_s, and E_i are the area of the simulated plate, the wavelength of the incident EM wave, the electric field strength of the transmitted and received waves, respectively.

Fig. S1

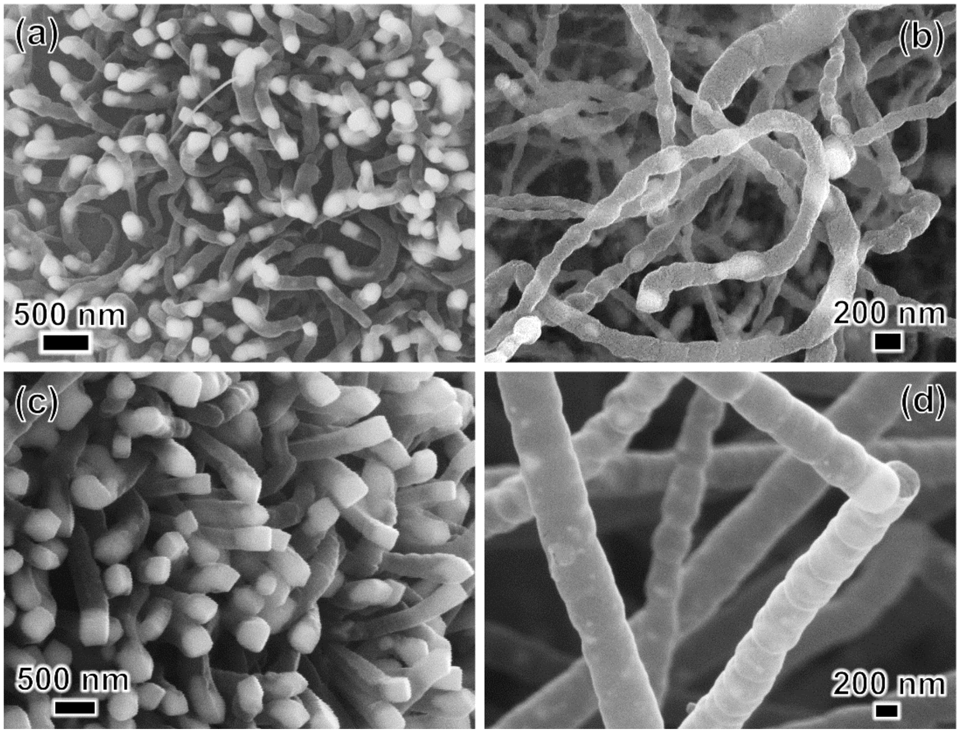

Fig. S1 SEM images of **a** short CNTs and **b** long CNTs of NNCF-1; **c** short CNTs and **d** long CNTs of NNCF-3

Fig. S2

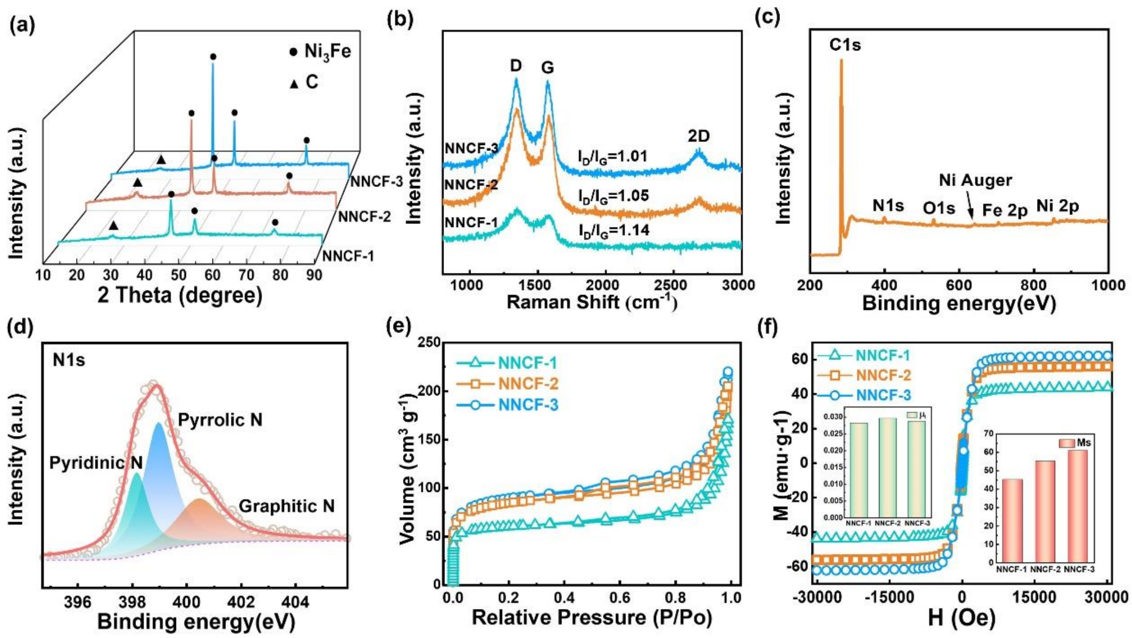

Fig. S2 a XRD patterns; **b** Raman spectrum; **e** Nitrogen sorption isotherms; **f** magnetic hysteresis loops of three samples; **c** XPS survey spectra; **d** high-resolution XPS spectrum for N 1s of NNCF-2

In Fig. S2a, it is easy to find that the diffraction peaks lie in 26.5°are indicated to be CNT (JPCDS: 89-7213). As for all products, the prominent peaks at 44.2°, 51.5°, and 75.8° are well-indexed to the (111), (200) and (220) planes of Ni_3Fe alloy (JPCDS: 88-1715), respectively.

The bionic neural network takes carbon as the main framework, and Raman spectroscopy is used to characterize the bonding state of carbon (Fig. S2b). The distinct characteristic peaks at 1350 cm^{-1} (D band) are related to topological vacancies and defects of the samples, and these vacancies and defects are conducive to the formation of electric dipoles. In this case, I_D/I_G values are 1.14, 1.05, and 1.01 for NNCF-1, NNCF-2 and NNCF-3, respectively, indicating the increase of crystalline carbons with rising temperatures, which is conducive to boost conductivity and support the proof of effective control of conduction loss.

The XPS survey scan of NNCF-2 in Fig. S2c reveals the presence of C, N, O, Ni and Fe elements in the hybrid nanostructure. The nitrogen heteroatoms and many curls and folds of graphite layers on the short CNTs destroy the balanced charge distribution on the original carbon lattice and promote the formation of polarization centers, providing an additional dipole polarization loss.

NNCF-1/NNCF-2/NNCF-3 display a type-IV isotherm curves with a distinct hysteresis loop, suggesting the typical mesoporous structure which corresponds to BET surface areas of 200.4 m^2/g, 272.3 m^2/g, and 310.1 m^2/g (Fig. S2e), respectively. With higher pyrolysis temperature, the BET surface areas increase due to the acceerative growth of CNTs to construct more developed porous conductive network to greatly facilitate the transmission of electrons, multiple reflection and low density. Such well-developed pore structure contributes to regulate impedance matching for relieving the reflection of EMW.

Furthermore, three samples exhibit good soft magnetic behavior benefiting from the intrinsic high saturation magnetization and the low magneto-crystalline anisotropy constant of Ni_3Fe (Fig. S2f). The saturated magnetization values (M_s) of NNCF-1, NNCF-2, and NNCF-3 are 45.3, 55.2, and 61.0 $emu \cdot g^{-1}$, and the initial permeability (μ_i) is 28.2, 29.6 and 28.7 emu/(g·kOe), respectively. This upward tendency was ascribed to the incremental crystallization and size of magnetic components with the increasing temperatures. Apparently, NNCF-2 possesses a moderate saturation magnetization, a highest initial permeability, coupled with its lowest intrinsic coercivity (H_c=101.8 Oe), and therefore it is favorable to magnetic polarization and corresponding magnetic loss ability by maximum advantage under the weak component of magnetic field in incident EMW.

Fig. S3

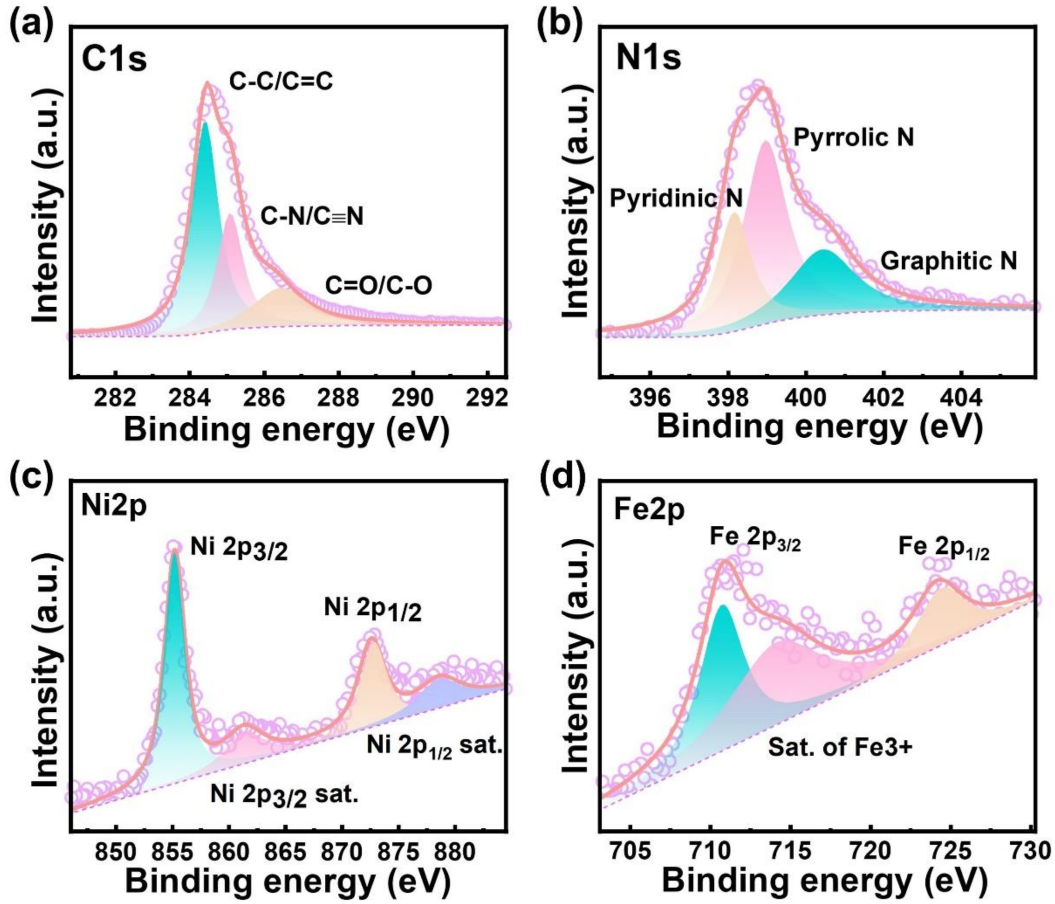

Fig. S3 XPS spectra of **a** C1s; **b** N1s; **c** Ni2p and **d** Fe2p of NNCF-2 composite

Fig. S4

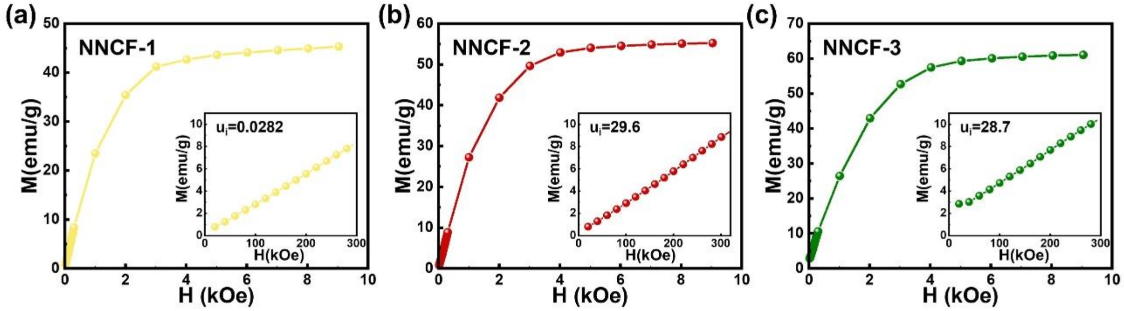

Fig. S4 The initial permeability of **a** NNCF-1; **b** NNCF-2; **c** NNCF-3

Fig. S5

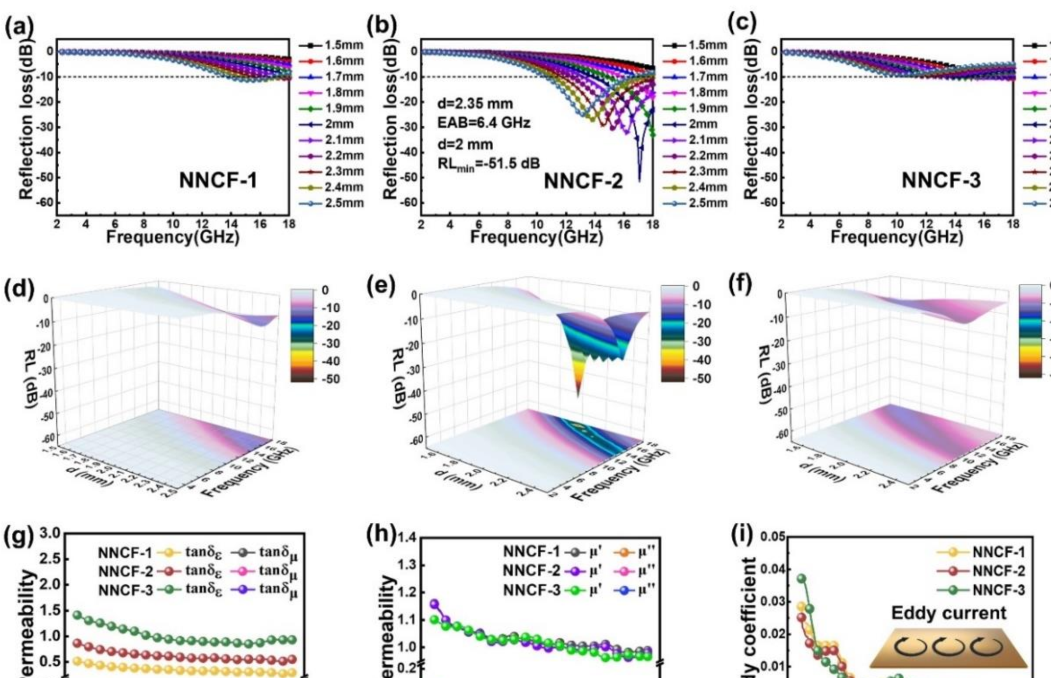

Fig. S5 Dependence of RL values on the thickness of **a, d** NNCF-1; **b, e** NNCF-2 and **c, f** NNCF-3 with the filling ratio 10 wt% during 2-18 GHz; **g** dielectric and magnetic loss angle tangent of three samples; **h** the real and imaginary parts of the permeability of NNCF-1, NNCF-2 and NNCF-3; **i** eddy coefficient C_0 value of NNCF-1, NNCF-2 and NNCF-3

Therein, RL values ware characterized by equations based on transmission line theory according to openly announced research [1].

$$\mathrm{RL} = 20\lg\frac{|Z_{in}-Z_0|}{|Z_{in}+Z_0|} \tag{2}$$

$$Z_0 = \sqrt{\frac{\mu_0}{\varepsilon_0}} \tag{3}$$

$$Z_{in} = Z_0\sqrt{\frac{\mu_r}{\varepsilon_r}}\tanh\left[j\left(\frac{2\pi f d}{c}\right)\sqrt{\mu_r\varepsilon_r}\right] \tag{4}$$

where Z_0 is the characteristic impedance of free space, Z_{in} is the normalized input impedance of a metal-backed microwave absorbing layer, μ_0 and ε_0 is the permeability and the dielectric constant of free space, respectively, ε_r and μ_r is the measured relative permittivity ($\varepsilon_r = \varepsilon' - j\varepsilon''$) and permeability ($\mu_r = \mu' - j\mu''$), respectively, f is the frequency, c is the velocity of light, d is the thickness.

Besides, α is related to the EMW energy assimilated by the absorber and impedance matching Δ is associated with the degree that EMW propagates the inside of the absorber, which are evaluated by the following formulas [2]:

$$\alpha=\frac{\sqrt{2}\pi f}{c}\sqrt{(\mu''\varepsilon''-\mu'\varepsilon')+\sqrt{(\mu''\varepsilon''-\mu'\varepsilon')^2+(\mu'\varepsilon''-\mu''\varepsilon')^2}} \tag{5}$$

$$\Delta=\left|\sinh^2(kfd)-M\right| \tag{6}$$

$$K=\frac{4\pi}{c}\sqrt{\varepsilon'\mu'}\frac{\sin\left(\frac{\delta_\varepsilon+\delta_\mu}{2}\right)}{\sqrt{\cos(\delta_\varepsilon)\cos(\delta_\mu)}} \tag{7}$$

$$M=\frac{4\varepsilon'\cos(\delta_\varepsilon)\mu'\cos(\delta_\mu)}{(\mu'\cos(\delta_\varepsilon)-\varepsilon'\cos(\delta_\mu))^2\left(1+\tan^2\left(\frac{\delta_\mu-\delta_\varepsilon}{2}\right)\right)} \tag{8}$$

where δ_ε=arctan ($\varepsilon''/\varepsilon'$) and δ_μ= arctan (μ''/μ') are the dielectric loss and magnetic loss angle, respectively.

Fig. S6

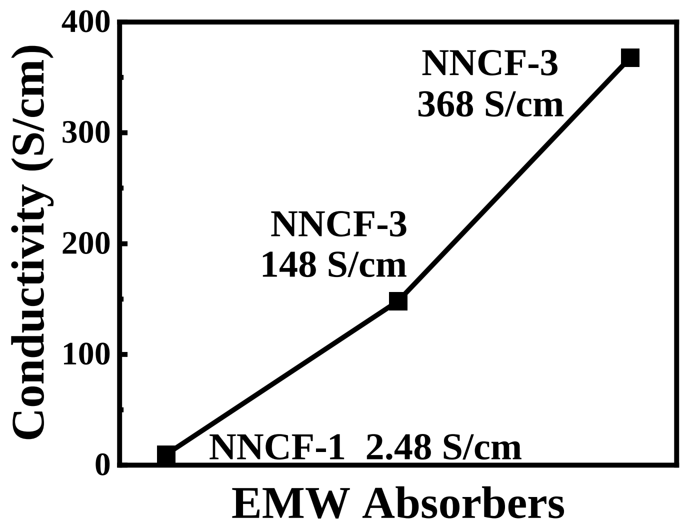

Fig. S6 The electrical conductivity of NNCF-1, NNCF-2 and NNCF-3

Fig. S7

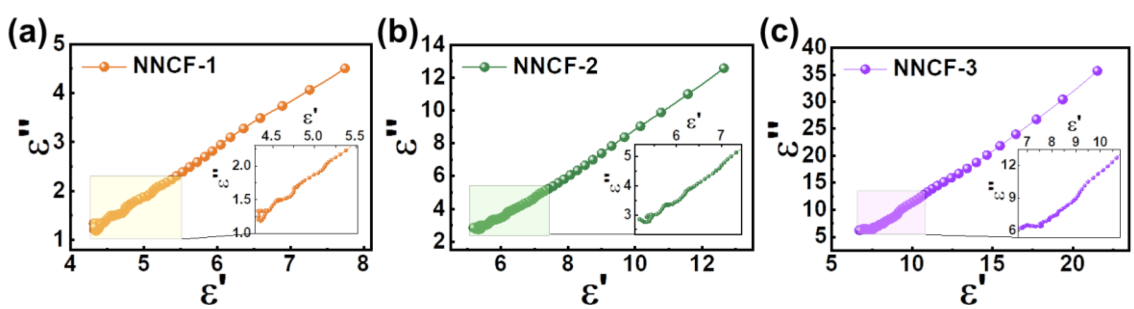

Fig. S7 Cole-Cole plots of **a** NNCF-1; **b** NNCF-2 and **c** NNCF-3 (The three insets are the local magnification of Cole-Cole semicircles in the high-frequency band for each sample, respectively)

Fig. S8

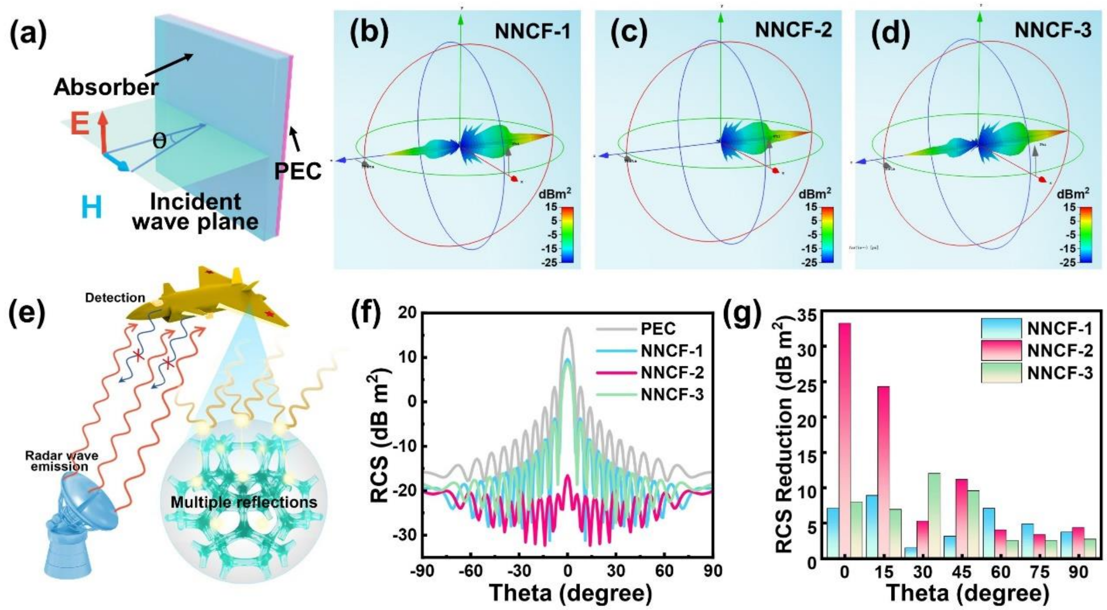

Fig. S8 **a** The model in the simulation; 3D RCS plot for the Perfect Electrical Conductor (PEC) substrate covered with **b** NNCF-1; **c** NNCF-2; **d** NNCF-3; **e** illustration on target detection of aircraft by radar; **f** RCS plots in the Cartesian coordinate system under certain detecting angles and **g** RCS reduction values for three samples

The radar cross section (RCS) of an ultra-thin PEC plate covered with Ni_3Fe@NCNT@CFs hierarchical bionic neural network as absorbers at different incident angles was simulated in the real far field condition by CST software. Fig. S8b–d represent the 3D radar wave scattering images, wherein similar 3D shapes but different scattering intensities of NNCF-1 to NNCF-3 absorbers are presented. The PEC absorber shows the strongest scattering signal, while the scattering signal of NNCF-2 is the smallest, meaning a good capacity in EMW attenuation, under which strong microwave scattering signals of the conductor are successfully suppressed. The comparison of two-dimensional RCS (Fig. S8f) shows that PEC as reflective substrate has the strongest reflection (no EMW absorption) and the NNCF-2 has the best absorption with minimum RCS signal (below −10 dBm^2) at all detection ranging from -90° to 90 °, superior to

NNCF-1 and NNCF-3. In order to more intuitively evaluate the intrinsic energy dissipation abilities of different coatings, the RCS reduction effect is harvested by removing the RCS value of the PEC substrate at certain detection angles (ranging from -90° to 90° in 15° increments). In Fig. S8g, all three samples make a beneficial contribution to reducing RCS and NNCF-2 has maximal RCS reduction at 0° (33.21 dBm^2). The RCS simulation results are consistent with their reflection loss and it unambiguously validates that our proposed conduction loss dominated bionic neural network-like NNCF-2 absorber promises a practical feasibility in the real-far-field stealth applications.

Fig. S9

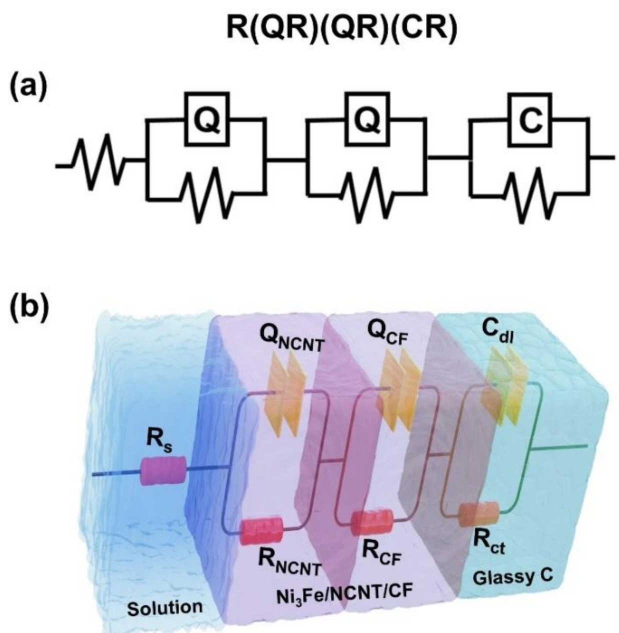

Fig. S9 Equivalent circuit of **a, b** NNCF-2 coating soaked in neutral 3.5wt% NaCl test environments for 720 hours (Here the circuit model is R(QR)(QR)(CR))

In Fig. S9b, the R_s on behalf of the solution resistance, Q_{CF}, Q_{NCNT} correspond to the constant phase element capacitance of carbon foam skeleton and CNT shell, R_{CF}, R_{NCNT}

correspond to the resistance of carbon foam skeleton and CNT shell, respectively. C_{dl} is the interface capacitance between the CNT shell and Ni_3Fe core and R_{ct} is the charge transfer resistance, describing the ability of diffusion for charged species in the interface area.

Fig. S10

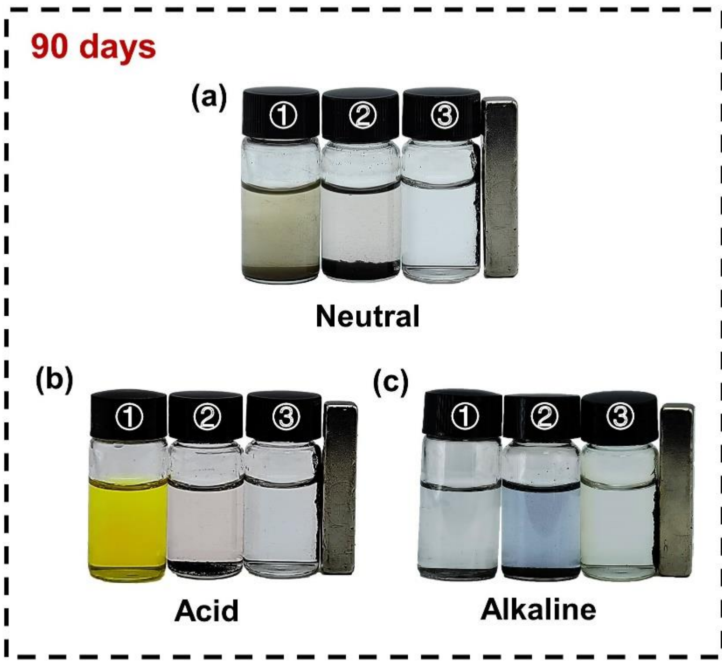

Fig. S10 NNCF-2 (right), together with CIP (left) and Co-MOF derivative (middle) immersed in three corrosive NaCl environments. **a** neutral; **b** acid; **c** alkaline. By contrast, NNCF-2 shows the most satisfactory corrosion resistance, comprehensively.

To affirm the anti-corrosion effects in an acid environment, the NNCF-2 (right), CIP (left) and Co-MOF derivative (middle) were dipped into NaCl acid solution (3M HCl) for an accelerated corrosion test (inset of Fig. S10b). The CIP is dissolved completely after one day, resulting in a canary yellow solution. For Co-MOF derivative, the solution becomes light pink due to the formation of Co^{2+}. In contrast, the NNCF-2 solution has no color change and still remain magnetism after 60 days. Soaking results in neutral and alkaline environments are demonstrated in Figs. S10a and S10c.

To summarize, the corrosive substances (Cl^-, O_2 and H_2O) in simulative seawater solution were resisted by the chemically inherent inert and impermeable CNT nanoshell network integrating 3D carbon foam neural network-like framework as resistance-like and capacitance-like robust shield, displaying high levels of corrosion protection (low I_{corr}, large R_p and R_{ct}). Thus, the active Ni_3Fe cores are protected from H_2O, O_2, and Cl^- attacking, and thus immensely mitigate the corrosion.

Table S1 Comparison of EMW absorbing performances of related advanced CF or CNT incorporated microwave absorbents (MAMs)

Absorbents	**Filler loading** [wt%]	**Maximum RL** [dB][a)]	**Thickness** [mm]	**EAB** [GHz][b)]	**Refs**
CF/Ni	25	-45	2	5.1	[2]
CF/Fe_3O_4	30	-26.45	5	4.28	[3]
CF/CuNi	40	-50.2	1.6	2.5	[4]
Fe_3O_4@$Ti_3C_2T_x$/CNTs	20	-40.1	2	5.8	[5]
CF/CoNi@C	20	-60	1.6	6.07	[6]
CF/Co@C	20	-59.82	2.3	5.64	[7]
CF/Co	30	-46.2	2	4.8	[8]
CF/CNTs/Fe_3C/Fe_3O_4	20	-40.47	2.11	6.0	[9]
CF/Ni/CNT	30	-47.0	1.8	5.8	[10]
CF/$NiCo_2O_4$	40	-63.6	2.8	4.72	[11]
CoNi@G@NCNTs	55	-54	2.5	5.2	[12]
Co@NCNT	25	-53.0	1.8	6.2	[13]
Co_1Zn_1@HNCNTS	20	-44.2	1.7	4.8	[14]
MWCNT/Ni	60	-37.0	5.2	2.1	[15]
MWCNT/Fe	60	-39.0	4.3	2.7	[15]
MWCNT/Co	60	-37.0	5.3	2.8	[15]
CMT@CNT/Co	15	-52.2	2	5.1	[16]
Ni/SnO_2/MWCNT	75	-39.2	1.5	3.6	[17]
Fe_3O_4/ PPy/CNT	20	-25.9	3	4.5	[18]
FeNi@CNT/CNRs	20	-47	2.3	4.5	[19]
CoNi@NCNT	10	-55.62	1.45	4.25	[20]
$NiCo_2$/CNT	50	-25.5	1.3	4.4	[21]
CF/Ni_3Fe/NCNT	10	-51.5	2.35	6.4	herein

[a)] Maximum value of reflection loss; [b)] Effective absorption bandwidth

Table S2 Corrosion kinetic parameters of NNCF-2, CIP and Co/C coatings immersed in neutral 3.5 wt% NaCl solution for 720 hours, respectively

Sample	E_{corr} **[V]**	I_{corr} **[A cm^{-2}]**	β_a **[mV]**	β_c **[mV]**	R_p **[Ω]**
NNCF-2	0.03118	2.79E-08	86.53	-89.206	2.54E+07
CIP	-0.054788	3.28E-07	318.8	-76.362	7.83E+04
Co/C	-0.14277	2.26E-07	117.49	-116.27	1.17E+05

$$R_P = \frac{\beta_a \beta_c}{I_{corr} \ln(10)(\beta_a + \beta_c)}$$

Here, β_a and β_c are on behalf of the slopes of anodic and cathodic Tafel plots, respectively. It can be concluded from Table S2 that the value of I_{corr} is in the following order: $I_{corr\text{-}NNCF\text{-}2} < I_{corr\text{-}CIP} < I_{corr\text{-}Co/C}$, for R_p, $R_{p\text{-}NNCF\text{-}2}$ is the largest and $R_{p\text{-}CIP}$ is the smallest. In general, I_{corr} and R_p can be used as parameters for qualitatively judging the anti-corrosion property of the coating, [22] the smaller the value of I_{corr}, the better anti-corrosion property of the coating while for R_p, the smaller, the worse. Hence, it can be preliminarily confirmed that the anti-corrosion property of the NNCF-2 coating was the most favorable.

Table S3 Equivalent circuit parameters of the NNCF-2 coating with the passage of soaking time in the neutral 3.5 wt% NaCl environment

R(QR)(QR)(CR)

NNCF-2	**3h**	**24h**	**168h**	**360h**	**720h**
R_s [Ω cm^2]	51.18	42.98	34.19	31.34	30.26
CPE_{NCNT} [F cm^{-2}]	5.652E-5	6.638E-5	1.274E-4	7.657E-5	1.298E-4
n	0.7868	0.8203	0.6119	0.8299	0.8108
R_{NCNT} [Ω cm^2]	1075	1164	1048	986.4	900.6
CPE_{CF} [F cm^{-2}]	2.063E-4	1.16E-4	7.133E-5	3.282E-4	1.289E-4
n	0.4878	0.5994	0.8159	0.6295	0.7201
R_{CF} [Ω cm^2]	450.2	374.4	354.2	323.1	260.5
C_{dl} [F cm^{-2}]	2.928E-5	1.094E-5	1.034E-4	1.622E-4	1.207E-4
R_{ct} [Ω cm^2]	8.542E5	7.786E5	7.345E5	7.042E5	6.965E5

References

1. Wang FY, Liu YL, Zhao HH, Cui LR, Gai LX, Han XJ, Du YC (2022) Controllable seeding of nitrogen-doped carbon nanotubes on three-dimensional Co/C foam for enhanced dielectric loss and microwave absorption characteristics. Chem. Eng. J. 450： 138160. https://doi.org/10.1016/j.cej.2022.138160

2. Sun QY, Shi JY, Wu LP, Wu F, Xie AM (2021) Ni@Carbon nanocomposites with hierarchical three-dimensional network for electromagnetic waves absorption. Ceram. Int. 47:27577–27585. https://doi.org/10.1016/j.ceramint.2021.06.182

3. Jiang S, Qian K, Yu KJ, Zhou HF, Weng YX, Zhang ZW (2021) Study on ultralight and flexible Fe_3O_4/melamine derived carbon foam composites for high-efficiency microwave absorption. Chem. Phys. Lett. 779:138873. https://doi.org/10.1016/j.cplett.2021.138873

4. Lu LF, Wang FL, Zhang X, Qiao J, Liu C,Liu JR (2021) CuNi alloy/ carbon foam nanohybrids as high-performance electromagnetic wave absorbers. Carbon 172: 488-496. https://doi.org/10.1016/j.carbon.2020.10.021

5. Zhang C, Wu ZC, Xu CY, Yang BT, Wang L, You WB, and Che RC (2022) Hierarchical $Ti_3C_2T_x$ MXene/carbon nanotubes hollow microsphere with confined magnetic nanospheres for broadband microwave absorption. Small 18:2104380. https://doi.org/10.1002/smll.202104380

6. Wang MQ, Wei B, Zhou JT, Yao ZJ, Xu LL, Zhang XF, Tao JQ, Shi ZJ (2022) Multi-scale CoNi nano-alloy/CoNi@C microsphere/3D macropores N-doped carbon foam composites: Lightweight and efficient electromagnetic wave absorption characteristics. Mater. Chem. Phys. 279:125777.

https://doi.org/10.1016/j.matchemphys.2022.125777

7. Gu WH, Tan JW, Chen JB, Zhang Z, Zhao Y, Yu JW, Ji GB (2020) Multifunctional bulk hybrid foam for infrared stealth, thermal insulation, and microwave absorption. ACS Appl. Mater. Interfaces 12:28727−28737. https://doi.org/10.1021/acsami.0c09202

8. Shi HG, Wang T, Cheng JB, Zhao HB, Li SL, Wang YZ (2021) Ultralow-density carbon foam composites with bean-like Co-embedded carbon nanotube whiskers towards high-performance microwave absorption. J. Alloys Compd. 863:158090. https://doi.org/10.1016/j.jallcom.2020.158090

9. Jia TM, Qi XS, Wang L, Yang JL, Gong X, Chen YL, Qu YP, Peng Q, Zhong W (2023) Constructing mixed-dimensional lightweight flexible carbon foam/carbon nanotubes-based heterostructures: An effective strategy to achieve tunable and boosted microwave absorption. Carbon 206:364–374. https://doi.org/10.1016/j.carbon.2023.02.046

10. Liu DW, Yang L, Wang FY, Zhang H, Liu J, Lv T, Zhao HJ, Du YC (2022) Hierarchical carbon nanotubes@Ni/C foams for high-performance microwave absorption. Carbon 196:867–876. https://doi.org/10.1016/j.carbon.2022.05.057

11. Zheng SN, Lyu LF, Wang FL, Liu Y, Liu JR (2021) Self-supported construction of three-dimensional $NiCo_2O_4$ hierarchical nanoneedles for high-performance microwave absorption. Ceram. Int. 47:34289–34296. https://doi.org/10.1016/j.ceramint.2021.08.339

12. Guo D, Yuan HR, Wang XC, Zhu CL, Chen YJ (2020) Urchin-like amorphous nitrogen-doped carbon nanotubes encapsulated with

transition-metal-alloy@graphene core@shell nanoparticles for microwave energy attenuation. ACS Appl. Mater. Interfaces 12:9628–9636. https://doi.org/10.1021/acsami.9b20412

13. Huang MQ, Wang L, Pei K, You WB, Yu XF, Wu ZC, Che RC (2020) Multidimension-controllable synthesis of MOF-derived Co@N-Doped carbon composite with magnetic-dielectric synergy toward strong microwave absorption. Small 16:2000158. https://doi.org/10.1002/smll.202000158

14. Li KY, Sun H, Zhang X, Zhang S, Dong HW, Zhu CL, Chen YJ (2020) Micro-nanospheres assembled with helically coiled nitrogen-doped carbon nanotubes: Fabrication and microwave absorption properties. Mater. Des. 186 108290. https://doi.org/10.1016/j.matdes.2019.108290

15. Wen FS, Zhang F, Liu ZY (2011) Investigation on microwave absorption properties for multiwalled carbon nanotubes/Fe/Co/Ni nanopowders as lightweight absorbers. J. Phys. Chem. C 115:14025–14030. https://doi.org/10.1021/jp202078p

16. Wu ZC, Pei K, Xing LS, Yu XF, You WB, Che RC (2019) Enhanced microwave absorption performance from magnetic coupling of magnetic nanoparticles suspended within hierarchically tubular composite. Adv. Funct. Mater. 29: 1901448. https://doi.org/10.1002/adfm.201901448

17. Lin L, Xing HL, Shu RW, Wang L, Ji XL, Tan DX, Gan Y (2015) Preparation and microwave absorption properties of multi-walled carbon nanotubes decorated with Ni-doped SnO_2 nanocrystals. RSC Adv. 5:94539-94550. https://doi.org/10.1039/C5RA17303E

18. Yang R-B, Reddy PM, Chang C-J, Chen P-A, Chen J-K, Chang C-C (2016) Synthesis

and characterization of Fe_3O_4/polypyrrole/carbon nanotube composites with tunable microwave absorption properties: Role of carbon nanotube and polypyrrole content. Chem. Eng. J. 285:497-507. https://doi.org/10.1016/j.cej.2015.10.031

19. Xu XQ, Ran FT, Lai H, Cheng ZJ, Lv T, Shao L, Liu YY (2019) In situ confined bimetallic metal–organic framework derived nanostructure within 3D interconnected bamboo-like carbon nanotube networks for boosting electromagnetic wave absorbing performances. ACS Appl. Mater. Interfaces 11:35999–36009. https://doi.org/10.1021/acsami.9b14754

20. L-L Liang, Z Liu, L-J Xie, J-P Chen, H Jia, Q-Q Kong, G-H Sun, C-M Chen (2021) Bamboo-like N-doped carbon tubes encapsulated CoNi nanospheres towards efficient and anticorrosive microwave absorbents. Carbon 171:142-153. https://doi.org/10.1016/j.carbon.2020.08.057

21. Wang BC, Zhang C, Mu CP, Yang RL, Xiang JY, Song JF, Wen FS, Liu ZY (2019) Enhanced electromagnetic wave absorption properties of $NiCo_2$ nanoparticles interspersed with carbon nanotubes. J. Magn. Magn. Mater. 471:185-191. https://doi.org/10.1016/j.jmmm.2018.09.090

22. D Prasai, JC Tuberquia, RR Harl, GK Jennings, KI Bolotin (2012) Graphene: Corrosion-inhibiting coating. ACS Nano 6:1102–1108. https://doi.org/10.1021/nn203507y